Solar Cycle Variation of Coronal Temperature, Emission Measure, and Soft X-Ray Irradiance Observed with Yohkoh Soft X-Ray Telescope

Aki Takeda[1], Loren Acton[1], and Nicole Albanese[2]

[1] Dept. of Physics, Montana State University, P.O. Box 173840, Bozeman, MT 59717, USA; takeda@solar.physics.montana.edu

[2] Dept. of Physics and Astronomy, Tufts University, Medford, MA 02155, USA

Abstract

This paper presents the solar soft X-ray irradiance (0.3–3.0 nm) obtained from the mission-long full-Sun X-ray images observed with the Soft X-ray Telescope (SXT) of the Yohkoh mission (1991–2001). The irradiance was calculated using filter-ratio temperatures and emission measures (EMs) from the full-Sun integrated X-ray signals employing a coronal spectrum synthesized with CHIANTI atomic database version 8.0. Dependence of the results on the assumption of elemental abundances is investigated. The SXT irradiance for a shorter wavelength range was also calculated and compared with the low energy flux (0.1–0.8 nm) of the X-Ray Sensor on board the *GOES* satellite. To incorporate the spatial information of the observed corona, we tried the alternative method to derive irradiance by applying the filter-ratio method to the images of northern hemispheric corona instead of spatially integrated signals from there. The EM weighted average of the spatially resolved temperatures turned out to be generally 20%–30% lower than those derived from the integrated signals, while the total of spatially resolved EMs are accordingly 1.5–2 times higher. This trend is enhanced when solar activity is the lowest in early 1996. The irradiance obtained from the alternative method does not significantly vary from the result from the integrated signals. This provides some validation for the simpler full-Sun integrated method. The temporal variation of the EMs of cool (<1.5 MK), medium, and hot (>2.5 MK) components indicates that the ratio of the hot component relative to the medium component is higher in the ascending phase (mid 1998–2001) than in the descending phase (1992–1995) of the solar activity cycle.

Unified Astronomy Thesaurus concepts: Solar corona (1483); Solar spectral irradiance (1501); Solar X-ray emission (1536)

1. Introduction

Soft X-ray radiation from the Sun is the primary source of energy that produces free electrons in the ionosphere. The precipitous rise of ionospheric electron density may trigger widespread problems to our modern life, i.e., disrupting radio communication, increasing low-orbit satellite drag, degrading positioning accuracy with GPS satellites, etc. Besides these issues of practical importance, monitoring solar soft X-ray irradiance for a long period of time is valuable as the record of the activity cycle of a main-sequence star of the spectral type G2. Studying the Sun and its magnetic variability gives us an understanding of the processes of other stars.

The soft X-ray telescope (SXT) on board the Yohkoh satellite observed the Sun through the descending phase of Cycle 22 and the rising phase of Cycle 23 (Ogawara et al. 1991; Tsuneta et al. 1991). The SXT was the only imager of the Sun in the soft X-rays (0.3–3.0 nm) throughout its operating period, 1991 September through 2001 December. The SXT was equipped with five broadband X-ray filters, which are designed to diagnose coronal plasma of the temperature from under 1 MK to over 10 MK.

The initial attempt to derive the soft X-ray irradiance from the SXT data was performed in Acton et al. (1999). They showed that the temperatures of various coronal structures obtained by the filter-ratio method (for its application to SXT data, see Hara et al. 1992) were generally in good agreement with the the mean temperature of observed differential emission measures (EMs) collected by Bruner & McWhirter (1988). However, the final product of SXT irradiance data was not published, because the further calibration of visible stray light

contamination turned out to be crucial for the determination of the signals from the mission-long X-ray filter images. Peres et al. (2000) applied the filter-ratio method to the SXT full-Sun images to derive the temperature variation of the EMs integrated along the line of sight. The object of their work is to translate SXT observations into a format of stellar observation by X-ray instruments. Their analyses are based on seven pairs of images observed from 1992 to 1994 and not intended to study the variation over the whole activity cycle.

After Yohkoh ceased its scientific operation in 2001, all usable data products from the Yohkoh project were recalibrated, classified, and maintained in the Yohkoh Legacy data Archive (YLA; Takeda et al. 2009), which is the source of data of this work. The SXT data in the YLA has a significant advantage over those regularly archived along the mission in the following respects: (1) Correction of the stray light contamination and the satellite attitude database were significantly improved (Acton 2016). (2) CCD gain was updated to 90 electrons DN^{-1} from its initial value of 100 electrons DN^{-1} (Acton 2016). (3) SXT response functions were updated using more recent atomic data (Takeda 2011). The CHIANTI ver. 8.0 (Del Zanna et al. 2015) was used for this work, whereas SXT's former official response functions were based on Mewe et al. (1985, 1986). (4) Most recent correction of the SXT response functions considering the diminishing X-ray sensitivity experienced during the first 15 months of the mission (Acton 2018) was implemented. (5) Analysis software was upgraded in accordance with these changes.

In this paper, we present the solar soft X-ray irradiance obtained from the mission-long full-Sun X-ray images from the YLA. The irradiance was derived through the filter-ratio

temperatures and EMs from the full-Sun integrated X-ray signals employing a coronal spectrum synthesized with CHIANTI atomic database version 8.0. The details of the data processing are described in Section 2. The wavelength range of our primary product is from 0.3 to 3 nm, where the SXT is most responsive. Observation with this wavelength range is unique and not observed by any other instruments during the period of the Yohkoh mission. The absolute values of X-ray irradiance substantially varies with the observed range of wavelength, although it is also affected by the assumed coronal spectral model and the instrumental response. The filter-ratio temperature (Te) and EM can describe more essentially the variation of coronal plasma than the irradiance. Section 3.1 is devoted to discuss the mission-long variation of Te and EM in the plane of $\log Te$ (K) and $\log EM$ (cm^{-3}). The dependence of our results on the assumption of elemental abundances is discussed in the Section 3.2.

For the purpose of making a comparison with existing observations, we calculate the irradiance for the similar wavelength range as the low energy channel of the X-Ray Sensor (XRS) on board the *Geostationary Operational Environmental Satellite* system (*GOES*) operated by the National Oceanic and Atmospheric Administration (NOAA). The yearly composite of XRS long channel flux from the primary *GOES* satellites (the "seamless" *GOES*/XRS data in the YLA) is used for the comparison (see Section 2.3 for details). Section 3.3 presents the results of the comparison.

The use of full-Sun integrated signals for the irradiance study gains a photometrical advantage, but trades off the spatial information of the observed corona. To incorporate the spatial information, we try the alternative method that applies the filter-ratio method to the coronal images instead of spatially integrated signals. It is photometrically challenging, especially because SXT has experienced the stray light contamination since 1992 November. However, the Sun is the only star for which we can resolve the main body of coronal emission. The comparison of the two approaches may provide an important perspective to interpret other stellar data. In Section 4, we use only northern hemisphere data for the better photometry, and compare the results with the corresponding values derived from the spatially integrated signals.

2. Data Processing

2.1. Preparation of Irradiance Data

This work uses Level 2 data products from the YLA, which are SXT full-Sun composite images observed with two thin X-ray analysis filters (i.e., the Al 1265A filter and the Al/Mg/Mn composite filter, hereafter as customary denoted as the Al.1 and the AlMg filters, respectively). Each image consists of two or three different exposures to increase the intensity range and remove detector saturation. Table 1 shows the statistics of the SXT Level 2 products. In rough translation, our work based on the 20 pairs of Al.1 and AlMg images obtained per day during the science operation of the Yohkoh mission. The steps of the image processing are as follows:

1. Image pair selection. The YLA SXT Level 2 data images were screened to remove those with telemetry loss, severe saturation due to flares and severe noise due to high energy particles, then made pairs of Al.1 and AlMg images obtained within a 10 minute difference.

Table 1
Data Statistics of SXT Level2 Products in the Yohkoh Legacy Data Archive

Year (1)	Number of Al.1 Images (2)	Number of AlMg Images (3)	Number of Available Pairs (4)	Number of Days with Pairs (5)	Average Number of Pairs per Day (6)
1991	3213	793	336	23	15
1992	14979	10070	6937	319	22
1993	10915	21189	8948	344	26
1994	10599	22216	8818	347	25
1995	8910	23411	7749	342	23
1996	10145	23514	8978	346	26
1997	9888	23549	9035	338	27
1998	7898	18495	6321	338	19
1999	5397	19040	3415	319	11
2000	4627	27209	3647	297	12
2001	4931	23154	2565	284	9
total	91502	212640	66749	3297	...

2. Collection of full-Sun signals. Sum up coronal intensities from both filter images included in the area within $1.2R_\odot$ from the disk center. Figure 1 shows the sample of the Al.1 and AlMg filter images, in which the areas outside $1.2R_\odot$ from the disk center were masked out.
3. Derive filter-ratio temperatures and EMs. Apply the filter-ratio method to each Al.1 and AlMg signal pair to obtain the full-Sun averaged temperatures (K) and volume EMs (cm^{-3}).
4. Isothermal coronal spectrum (lines and continuum) is calculated from the derived temperature and EM, using CHIANTI atomic database and software (ver. 8.0). So-called "hybrid" elemental abundances (`Sun_coronal_2012_schmelz_ext.abund`) are assumed in accordance with the assumption of SXT's default response functions.
5. Integrate the obtained spectrum over (0.3–3.0 nm) or another desired range (e.g., 0.1–0.8 nm) to derive the radiant intensity of the coronal plasma, then converted to the irradiance at the distance of 1 au in units of W m^{-2}.

2.2. Use of New SXT Response Functions

The calculation of filter-ratio temperatures and EMs was performed using the latest modified SXT response functions introduced by Acton (2018). The new response function corrects diminishing X-ray sensitivity during the first 15 months of the SXT operation, by assuming the accumulation of some absorbing material on the outer surface of SXT prefilter and partially absorbing X-rays. After the occurrence of the first prefilter failure in 1992 November, the effect of the X-ray absorption became less significant than that of stray light contamination on the SXT functions.

Figure 2 shows the temporal variation of the new SXT temperature response functions. The plots in the left column show the temporal variation from the start of the mission until 1992 October 25, which is shortly before the date the signature of the first prefilter failure started to appear on 1992 October 27. It is considered that the growth of the absorbing layer on the prefilter was most significant in this period and the response curves continuously decrease over time. The modification of the SXT response functions of this period was newly introduced
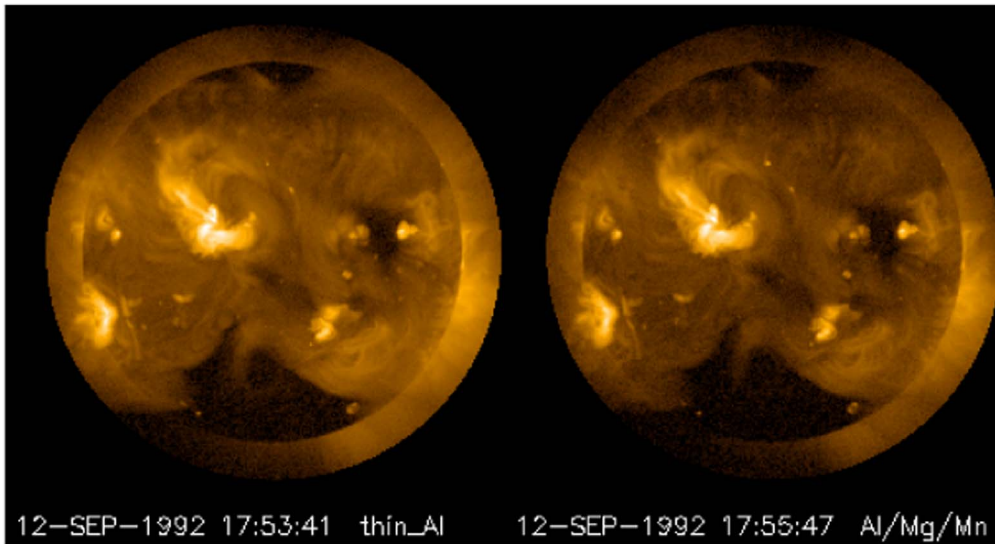
Figure 1. Sample SXT image pairs, images with the Al.1 filter (left) and the AlMg filter (right). The full-Sun integrated signals are collected from the area within $1.2R_{\odot}$. These pictures are displayed with logarithmically scaled intensities.

by Acton (2018). The plots of the right column show the variation after 1992 October 25 to the end of the mission. During this period, the response curves jump up at the time of the occurrence of a rupture (whose date is shown in the plots) and keep that level until the next rupture event. The growth of the absorbing material for this period was diminished to a negligible level. The modification of SXT response functions with respect to the stray light contamination had been applied in the previous studies. However, the sequence of prefilter failures was reexamined by Acton (2018) and the timing and the amount of correction have been improved in the latest version used in this work. Figure 3 shows the temporal variation of the filter-ratio function calculated as the AlMg response divided by the Al.1 response, which is referred to convert the obtained filter ratio to temperature.

2.3. The Seamless GOES/XRS Data at YLA

We utilized the seamless *GOES*/XRS data in comparison to the SXT irradiance with the *GOES*/XRS long channel flux (0.1–0.8 nm). The seamless *GOES*/XRS data archive (1991–2001) was prepared as a project of the YLA to add convenience for the studies of long-term variation of solar activity. A separate paper on this project is in preparation. Here we briefly describe their specification. They are essentially composite data from the primary *GOES* satellite of the time, based on the *GOES*/XRS data files under the Yohkoh database in the SolarSoft (Freeland & Handy 1998). The time resolution is 1 minute. The missing data periods of the primary satellite data (e.g., satellite eclipses or engineering) were replaced with those of a secondary satellite as much as possible. The scaling factors applied by Space Weather Prediction Center of NOAA to the archived flux were corrected (removed) to get true fluxes for 1991–2001. (See https://ngdc.noaa.gov/stp/satellite/goes/doc/GOESXRSreadme.pdf.)

3. Results

3.1. Solar Cycle Variation of SXT Irradiance, Te, and EM (1991–2001)

The SXT soft X-ray irradiance for the period, 1991 September through 2001 December calculated for the wavelength range,

0.3–3.0 nm is shown in Figure 4 together with the filter-ratio temperatures and EMs of the full-Sun integrated corona. These quantities were derived for each image pair then averaged (with no weight) to obtain daily values. These data are available from the YLA soft X-ray irradiance page at http://ylstone.physics.montana.edu/ylegacy/yla_sxirrad_acv/yla_sxirrad_acv.html. Over the whole mission period, coronal temperature smoothed over 14 days varies within a factor of 4 (most data points of logTe range from 6.1 to 6.7). On the other hand, EMs smoothed over the same period vary with a factor of ∼30, that is equivalent to the logEM range of ∼1.5. The EM is calculated from the filter-ratio temperature using the coronal signal from either image of the pair (the Al.1 image in this work) and the corresponding temperature response of the filter (see, Figure 2). When the derived temperatures (logTe) approached the value 7.0 at which the Al.1 filter has the highest response, the corresponding EMs are calculated low to explain the observed signal level. Such extraordinarily low EMs are observed in 1992, 1996, and 2001, associated with flare activities. The variation of irradiance extends over 2 orders of magnitude, showing similar variation with that of the original signals. The data points that have an outstandingly high temperature and low EM due to flare activities cancel each other out (although not completely) and result in a milder variation in the irradiance plot.

The uncertainty included in the irradiance derived from each pair of Al.1 and AlMg images was estimated through the following steps: (1) Uncertainties of signals. The YLA Level 2 uncertainty arrays corresponding to the selected Al.1 and AlMg images were used. These uncertainty arrays consider the errors introduced by decompression of the lossy compression algorithm and errors from the photon statistics (for details, see Section 2.10 of Acton 2016). Uncertainty of Al.1 and AlMg signals were calculated as the root sum square of the pixels of the uncertainty array corresponding to the studied area of each coronal image (i.e., within $1.2\ R_{\odot}$). The calculated uncertainty for each image is generally very small (less than 0.1%) for the full-Sun integrated signals. (2) Uncertainties of Te and EM were calculated by the IDL program, `sxt_teem.pro` as the propagation of the uncertainty of signals to the filter-ratios. The
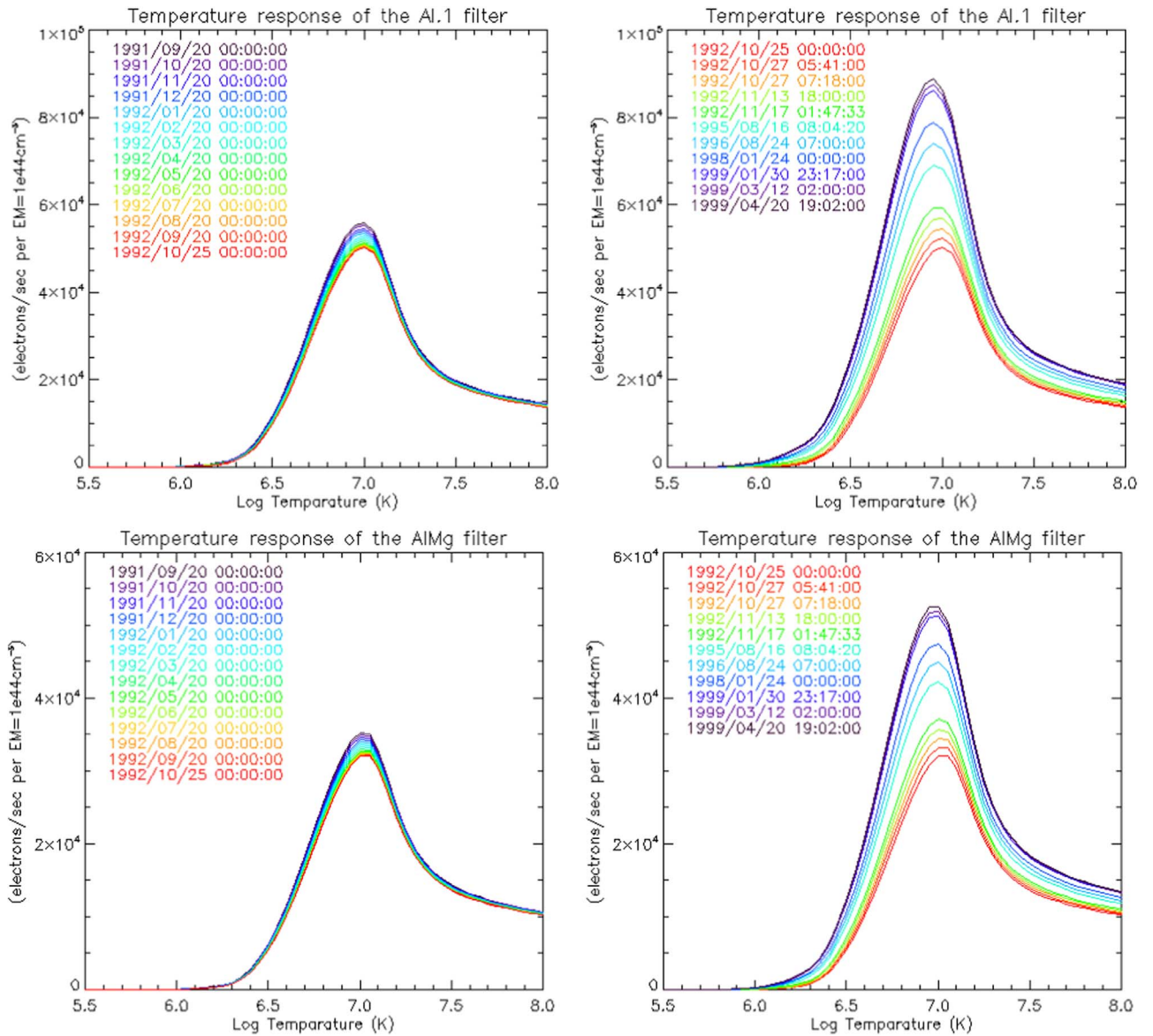
Figure 2. Temporal variation of SXT new temperature response functions for the Al.1 (top row) and AlMg (bottom row) filters. The right column shows the variation from the start of the mission to 1992 October 25, while the left column shows changes after 1992 October 25 until the end of the mission.

obtained uncertainties, d_Te and d_EM, differ with the phase of the mission, but roughly distributed around 0.2% and 0.8%, respectively. (3) Uncertainties of irradiance were estimated using the lower and higher limit of Te and the corresponding values for EM, defined as $Te\_lw = Te - d\_Te$, $Te\_hi = Te + d\_Te$, $EM\_lw = EM - d\_Te$, and $EM\_hi = EM + d\_Te$. The lower limit of the irradiance was defined as the irradiance calculated with Te_lw and EM_lw, while the higher limit was defined as the one calculated with Te_hi and EM_hi. The resulting uncertainty of the irradiance, defined as the ratio with the irradiance calculated with the original Te and EM, turned out to be 3% for both lower and higher cases.

SXT's standard routine for data reduction (`sxt_prep. pro`) corrects the visible stray light contamination, which the Al.1 filter images suffered most significantly since 1992 November. However, it is not included in the process of estimating uncertainty because there is no general way to quantify the amount of the error. In this work, we estimated the uncertainty of the stray light correction in the following way:

The uncertainty of the Al.1 signals was artificially increased to the value of 1.0%, while the uncertainty of AlMg signals remained unchanged. This increased uncertainty of Al.1 signals turned out to propagate to the uncertainty of *Te* and EM, as 1.5% and 6.0%, respectively. These increased uncertainties were used to estimate the uncertainty of the irradiance with the method described in step (3) above. The resulting uncertainty of the irradiance turned out to increase to the values 20%–30%. When we impose a harder condition by assuming the Al.1 signal uncertainty increased to 3.0%, the derived uncertainty of irradiance turns to the value of nearly 100% (a factor of two).

There are certainly other sources of uncertainties, as described in detail by Acton (2016). They are, however, difficult to quantify and not included in the uncertainties calculated by the standard routine: scattered X-rays and telescope vignetting are corrected in the standard routine, but the errors from these process are difficult to quantify. The uncertainty in CCD amplifier gain will be as large as 10%, and this directly propagates to the calculation of the EM and
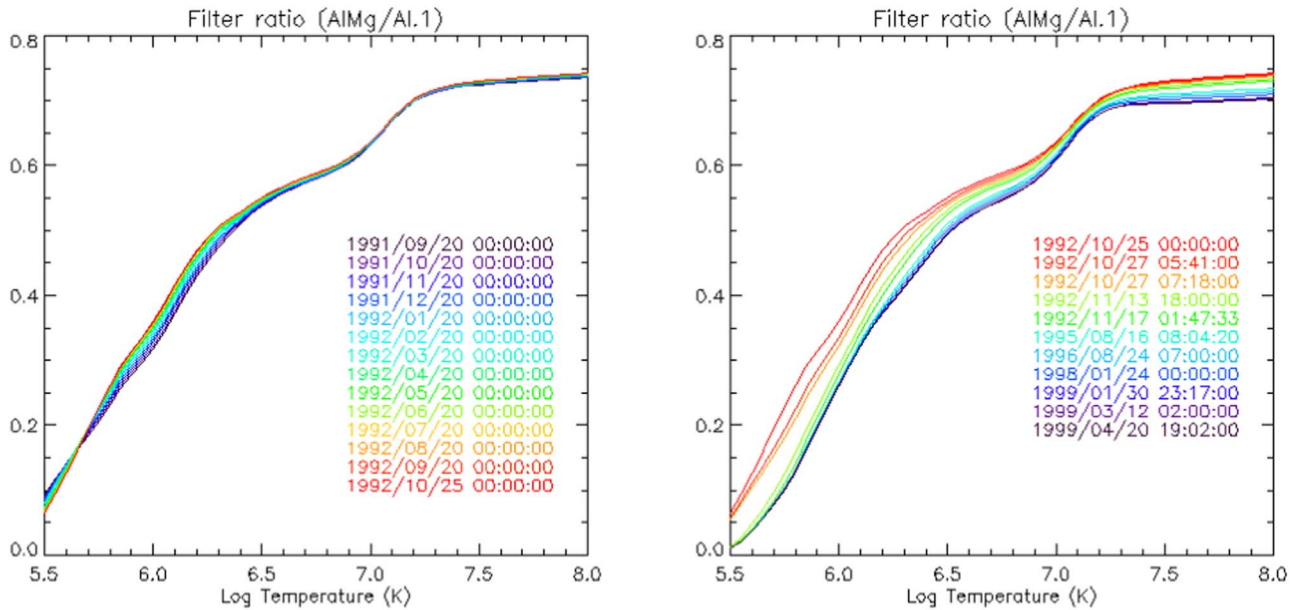
Figure 3. Temporal variation of filter-ratio function (AlMg/Al.1), for the same periods as those in Figure 2.

irradiance as the same amount of systematic error. There is an orbital drift in CCD dark current, caused by the UV flood operation performed at the beginning of every daylight pass to relieve the damage from ionizing radiation. This drift is corrected in the standard reduction routine with a few percent of uncertainty, which may be considerable when the signal level of data is extremely low.

Figure 5 shows the distribution of the daily averaged filter-ratio temperatures (Te) and and EMs in the form of a two-dimensional histogram. The bin size of the histogram along the Te-axis is 0.025 (K) in logarithmic scale, while the corresponding value along the EM-axis is 0.075 (cm^{-3}) in logarithmic scale. The yearly 2D histogram of every other year since 1992 indicates that near solar maximum (1992) data points (Te, EM) distributed at the position centered around (6.47, 49.7) in the plane of logTe and logEM, moving toward the position around (6.29, 48.9) at the solar minimum then turning back to the previous values at the maximum phase. It is noticeable that 1996 data points form a sharp edge at their lower left portion in parallel with the curves giving the same irradiance values (dotted curves in the plots of Figure 5). Those data points on the edge came from the periods when the Sun was free from active regions and had the least intensity fluctuation. During such periods, SXT signals were at the lowest level and thus small errors in signals had the highest impact on the temperature analysis. We consider that the edge was mainly formed by the intensity fluctuation of Al.1 images due to the stray light contamination, while the AlMg intensities were kept stable.

When the SXT signal level was the lowest, 40%–50% of the analyzed pixels in the image have a signal-to-noise ratio (defined as the intensity ratio of coronal to uncertainty data) less than 2. Such pixels are typically in the areas where the intensity, temperature, and EM are all low, and thus contribute insignificantly to the irradiance. However, we notice in several cases that the spiky noises in these areas contribute to raise the full-Sun averaged temperature and the resulting irradiance value. We therefore consider that the true minimum value of the SXT daily averaged irradiance may be lower than the value

shown in the plot for 1996 of Figure 5 (roughly $-5.6\,\mathrm{W\,m^{-2}}$ in log scale). A more reliable value of the minimum SXT irradiance can be obtained by the spatially resolved approach discussed in Section 4.

3.2. Choice of Elemental Abundances

The elemental abundance of the coronal plasma is assumed in the calculation of isothermal coronal spectra, which is used for the derivation of SXT irradiance and also for the preparation of SXT temperature response functions. In this work, we assumed the so-called "hybrid" abundance prepared by Schmelz et al. (2012) through the abundance file (`Sun_coronal_2012_schmelz_ext.abund`) provided by CHIANTI atomic database version 8.0 (Del Zanna et al. 2015). It is the current default setting of the SXT temperature analysis software prepared by the YLA.

Recently, Brooks & Baker (2017) reported that the FIP bias (ratio of coronal to photospheric abundances) of the global corona highly correlates with the F10.7 cm radio flux and thus solar magnetic activity. The FIP bias they derived was 2.5 when the solar activity was low in 2010, and it reached above 3.5 as the activity increased since 2012. It is therefore useful to compare the results obtained by assuming different types of elemental abundances. In this subsection, we make a comparison among the following three elemental abundance sets provided by the CHIANTI atomic database (for details, see the notes given at the end of each abundance file in the CHIANTI database).

1. `Sun_coronal_2012_schmelz_ext.abund`:
   Assumed by default in this work. The latest version of hybrid abundance set based on Schmelz et al. (2012). Denoted hereafter as "hybrid."
2. `Sun_coronal_1992_feldman_ext.abund`: Traditional coronal abundance set based on Feldman et al. (1992). Denoted as "coronal."
3. `Sun_photospheric_2011_caffau.abund`: The latest version of photospheric abundance set based on Caffau et al. (2011). Denoted as "photospheric."
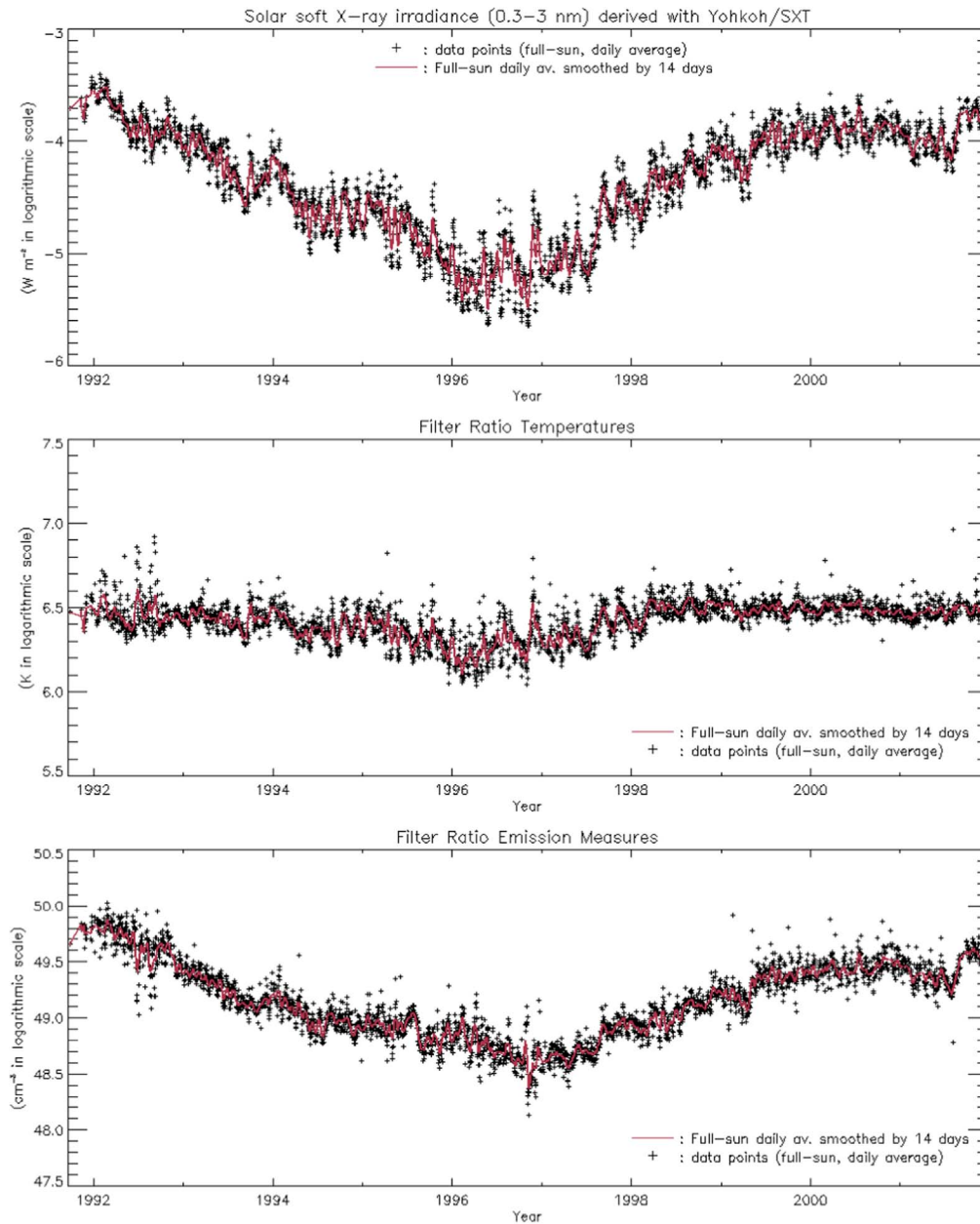
Figure 4. Mission-long variation of SXT irradiance for 0.3–3 nm (top plot), filter-ratio temperature (middle) and emission measure (bottom). Daily averaged data points (cross signs) and their smoothed data over the period of 14 days (red solid lines).

The different assumptions of elemental abundances affect the filter-ratio temperatures and EMs through the instrumental response function, which varies with the elemental abundances. Regarding the SXT, the relative positions of the filter-ratio curves derived from different abundance assumptions varies with the time of observation and also the temperature range of the observed data. Figure 6 shows the filter-ratio curves derived from the different abundance assumptions for 1992, 1996, and 2000, as sample years. For a given filter-ratio value, assuming the photospheric abundance tends to provide the lowest temperature. The coronal and hybrid abundances yield similar temperature values at higher temperature ranges ($\log Te > 6.4$), while coronal abundance results in a lower temperature at a lower temperature range.

The scatter plots of the daily averaged temperatures (Te) and EMs obtained from the above three different abundance sets are shown in Figure 7 for the same sample years as in Figure 6. The plotting range of Te and EM was set the same as in the plots in Figure 5. Compared with the results from assuming the hybrid abundance, 30%–45% lower EMs are calculated by assuming the coronal abundance. The photospheric abundance, on the contrary, yields 15%–30% higher EMs. These differences in Te and EM described in the above propagated to the SXT irradiance as follows: assuming the coronal abundance does not make significant difference or slightly (less than 5%) higher values than the irradiance with hybrid abundance. On the other hand, the photospheric abundance raises the irradiance 10%–20% higher than the hybrid case.

3.3. Comparison with GOES/XRS 0.1–0.8 nm Channel

Yohkoh/SXT is the unique source of solar soft X-ray irradiance of the wavelength range, 0.3–3 nm throughout the
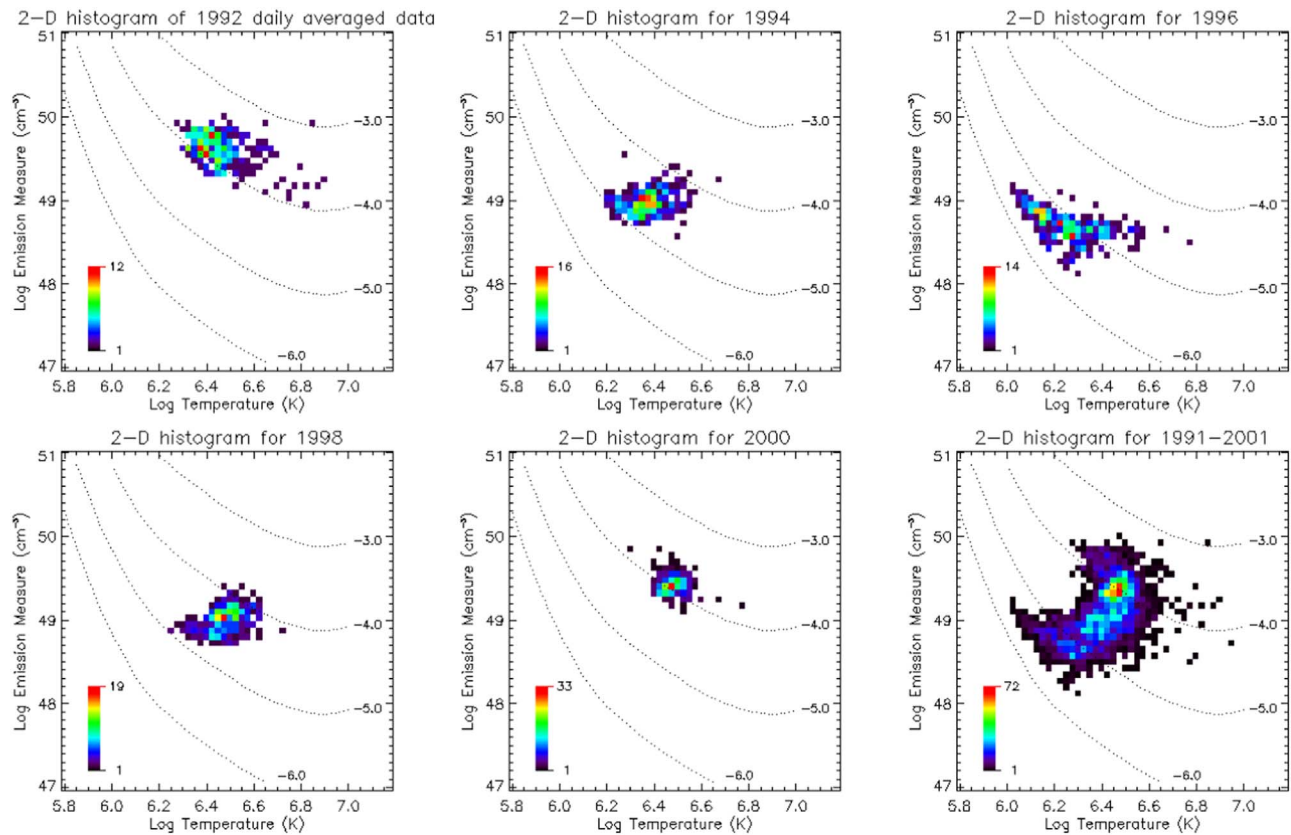
Figure 5. 2D histograms of daily averaged SXT filter-ratio temperatures and emission measures, for the years 1992, 1994, and 1996 (top row from left to right), and 1998, 2000, and 1991–2000 (bottom row from left to right). The bin size of the histogram along the Te- and EM-axes is 0.025 (K) and 0.075 (cm^{-3}), respectively, in logarithmic scale. The dotted curves indicate the pairs of Te and EM that give the same irradiance values; −3.0, −4.0, −5.0, and −6.0 W m^{-2} (in logarithmic scale), respectively.
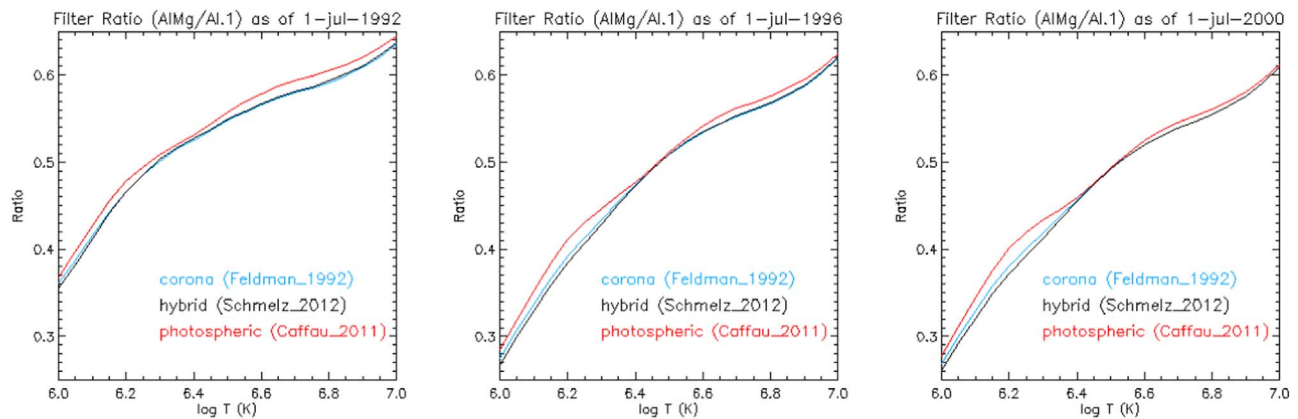
Figure 6. SXT temperature response functions with different elemental abundance assumptions for the years 1992 (left), 1996 (middle), and 2000 (right). The blue, black, and red lines denote "coronal," "hybrid," and "photospheric" abundances, respectively.

period of its operation. The only other source of long-term soft X-ray measurements is the XRS on board a series of *GOES* satellites, whose wavelength ranges are 0.05–0.4 nm (the short channel) and 0.1–0.8 nm (the long channel). To make a comparison, we calculated the SXT irradiance for the wavelength ranges similar to the long channel of *GOES*/XRS, then compared with the *GOES*/XRS long channel flux obtained from the YLA seamless *GOES*/XRS data archive at https://ylstone.physics.montana.edu/ylegacy/yla_seamless_goes.

We initially calculated the SXT irradiance for the wavelength range, 0.1–0.8 nm, as shown by the blue line in Figure 8. However, it turned out that the obtained irradiance is

significantly lower than that of XRS (black line in Figure 8). When the Sun's activity was high to moderate, the SXT irradiance is lower by a factor of 3–5. Around solar minimum (1995–1997), the soft X-ray flux often went under the detection limit of *GOES*/XRS, and thus the SXT irradiance has even lower (roughly a factor of 10) values than the flux observed by *GOES*/XRS.

We next calculated the wavelength range 0.03–1 nm, which is the width at 1% of peak response of *GOES*/XRS long channel, as shown in the left plot of Figure 9). This range is chosen in a way analogous to the case of SXT irradiance (the right plot of Figure 9). For this wavelength range, the SXT
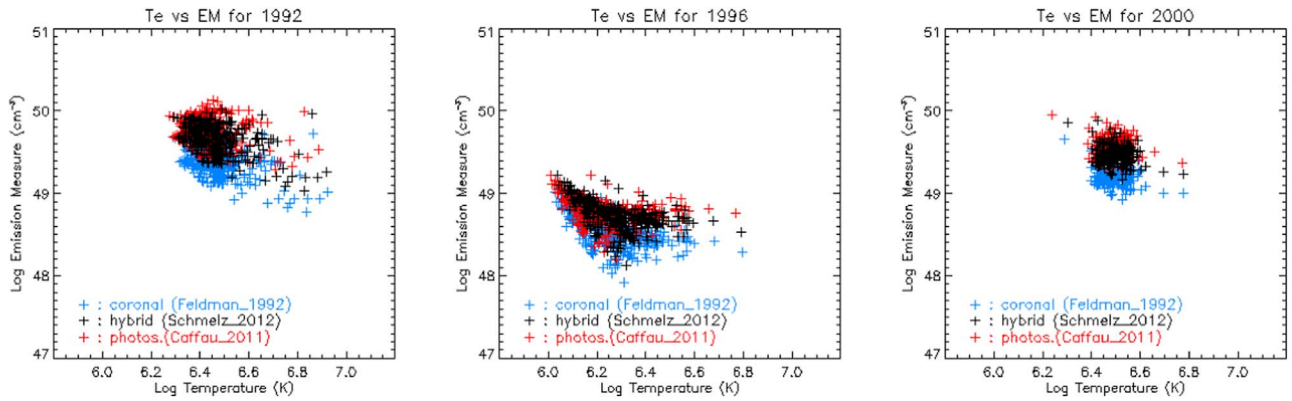
Figure 7. Scatter plot of daily averaged filter-ratio temperatures and emission measures with different elemental abundance assumptions. See the caption of Figure 6 for convention.
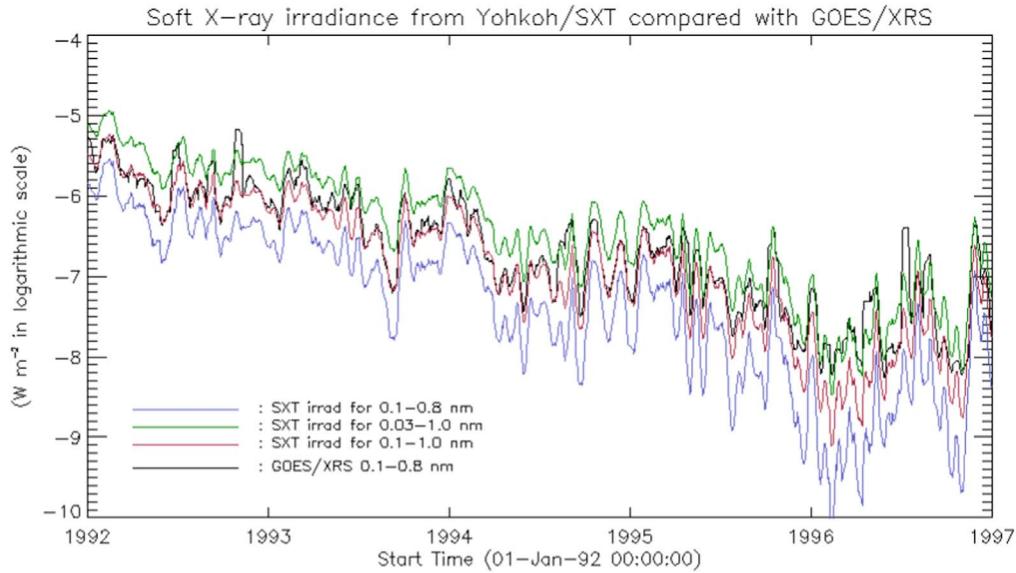

Figure 8. SXT daily averaged irradiances calculated for the wavelength ranges similar to *GOES*/XRS long channel for the period 1992–1997. The wavelength ranges are 0.1–0.8 nm (blue line), 0.03–1.0 nm (green line), and 0.1–1.0 nm (red line), compared with the daily averaged *GOES*/XRS long channel flux (black line).

irradiance is calculated significantly higher than the *GOES*/XRS by a factor of 2–4 outside the solar minimum. We also tried the calculation of the SXT irradiance applying the *GOES*/XRS response to the coronal spectra (at the step 5 in Section 2.1). However, the resulting irradiances for the 0.3–1.0 nm range yield significantly (more than a factor of 3) lower than the values of XRS irradiance. These large differences in the absolute irradiance values between SXT and XRS are not surprising. They are different types of instruments (SXT is an imager with CCD while XRS is an ion chamber) with different spectral response (Figure 9). In addition, the different spectral assumptions when converting the instrumental measurements to the physical unit of W m^{-2} may affect the derived values of irradiance. The SXT assumes an isothermal coronal spectrum, while the XRS assumes a flat spectrum.

As a practical measure, we found that the SXT irradiance calculated for 0.1–1.0 nm wavelength range (red line in Figure 8) provides comparable absolute level with the XRS irradiance apart from the period of solar minimum. The close comparison for the well-matched period shows that the major discrepancy comes from the height of peaks: XRS generally has higher peaks than those of SXT. It is reasonable because the source data for SXT irradiance do not include those during

flares due to saturation, while XRS does observe them. Another source of discrepancy lies in the different rate of data sampling: While the time resolution of XRS data is 1 minute, SXT full-Sun images used for this work were taken 10–20 pairs per day and missed many of the active events. This trend is especially pronounced later in the mission (1999–2001) when the number of image pairs became less than half of that earlier in the mission (e.g., 1992–1994, see Table 1 for the data statistics).

Figure 10 shows the mission-long comparison of SXT irradiance for 0.1–1.0 nm range with the XRS irradiance. In spite of the discrepancies noted above, they are generally in good agreement outside the period of solar minimum. This indicates that the SXT irradiance for the 0.1–1.0 nm range can be used as a proxy of the XRS irradiance when the solar activity level is under the detection limit of XRS.

4. Discussion

4.1. Disk-integrated versus Spatially Resolved Analysis

The derivation of coronal temperature and EM using full-Sun integrated signals has an advantage in the robustness of the results because of the high signal-to-noise ratio of the data by integration. However, this approach, which is equivalent to
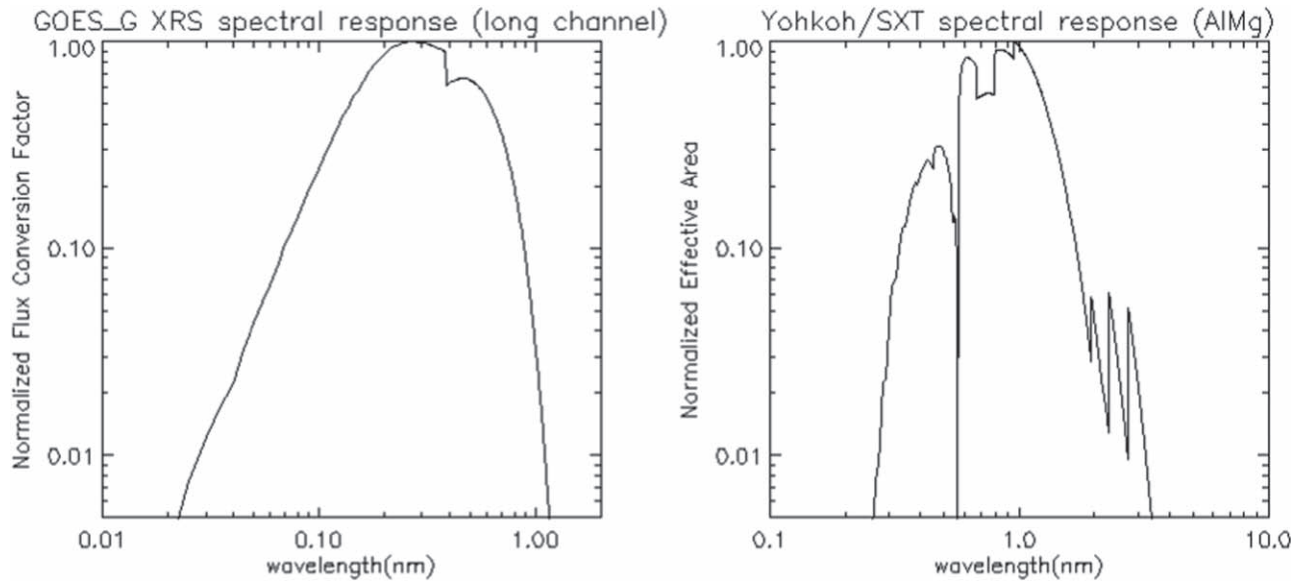
Figure 9. Normalized spectral responses of *GOES*/XRS long channel and Yohkoh/SXT AlMg filter. The *GOES* response (left) was prepared from the Calibration Report for XRS (https://ngdc.noaa.gov/stp/satellite/goes/doc/Document-02(Jan1985)_goesg_xrs_calibration.pdf), which is identical to the XRS on board the *GOES*-7. The flux conversion factor for the B Chamber (0.1–0.8 nm) was normalized by its peak value. The SXT response (right) was calculated from the SXT effective area function for the AlMg filter, by normalizing relative to its peak value.
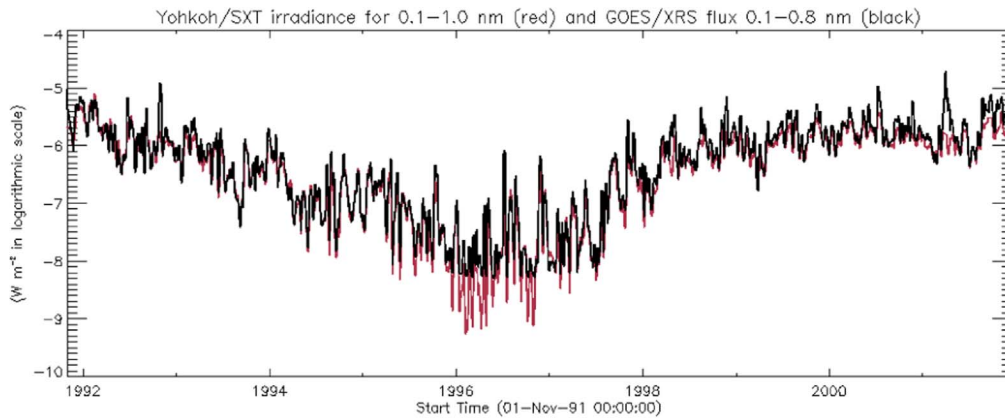

Figure 10. Mission-long variation of the SXT irradiance for 0.1–1.0 nm wavelength range compared with the XRS irradiance of the long channel. Both data are daily averaged and smoothed with a 14 day window.

observe the Sun as a star, imposes a crude assumption on the observed corona; temperature and EM at the time of observation are uniform not only along the line of sight, but also over the whole area in which the signals were collected. The Sun is the only star for which we can resolve its surface structures. It is naturally expected that the use of the spatial information will bring more realistic results on the observed corona. The comparison of the two approaches (full-Sun integrated signals versus spatially resolved data) might offer valuable insight for interpreting other stellar data. This section is devoted to describing our attempt to use the spatial information of SXT images in deriving coronal temperatures and EMs, then irradiance.

Applying the filter-ratio method to full-Sun images instead of integrated signals is photometrically challenging. To improve photometrical statistics, the pixel resolution of all the image pairs was rebinned to 9.8 arcsec pix^{-1}, with which SXT full-Sun images are the size of 256×256 pix. In addition, we used only the northern hemispheric area of each image for this work. The southern hemispheric corona was

masked out to avoid the southeast part of the image where major stray light patterns are located. We thereby obtained a mission-long series of temperature and EM maps of the northern hemispheric corona. For each pair of temperature and EM maps, we calculated the average temperature weighted by EMs, and the total EM as a sum of all pixels in an EM map. Using these averaged temperature and the total EM, the irradiance (0.3–3.0 nm) from the northern hemispheric corona was calculated with the same method used for the integrated signals. These quantities were daily averaged and plotted in Figure 11, compared with the results obtained from the spatially integrated signals.

It turned out that the averaged temperatures from the spatially resolved data are systematically lower than those from the integrated signals. It is generally lower by 20%–30% but reaches more than 50% around the solar minimum (top plot in Figure 11). This result is reasonable because the cooler component of the corona does not efficiently contribute to the integrated signals and is thus underestimated in the filter-ratio temperature derived from the integrated signals. In the method using spatially resolved data,
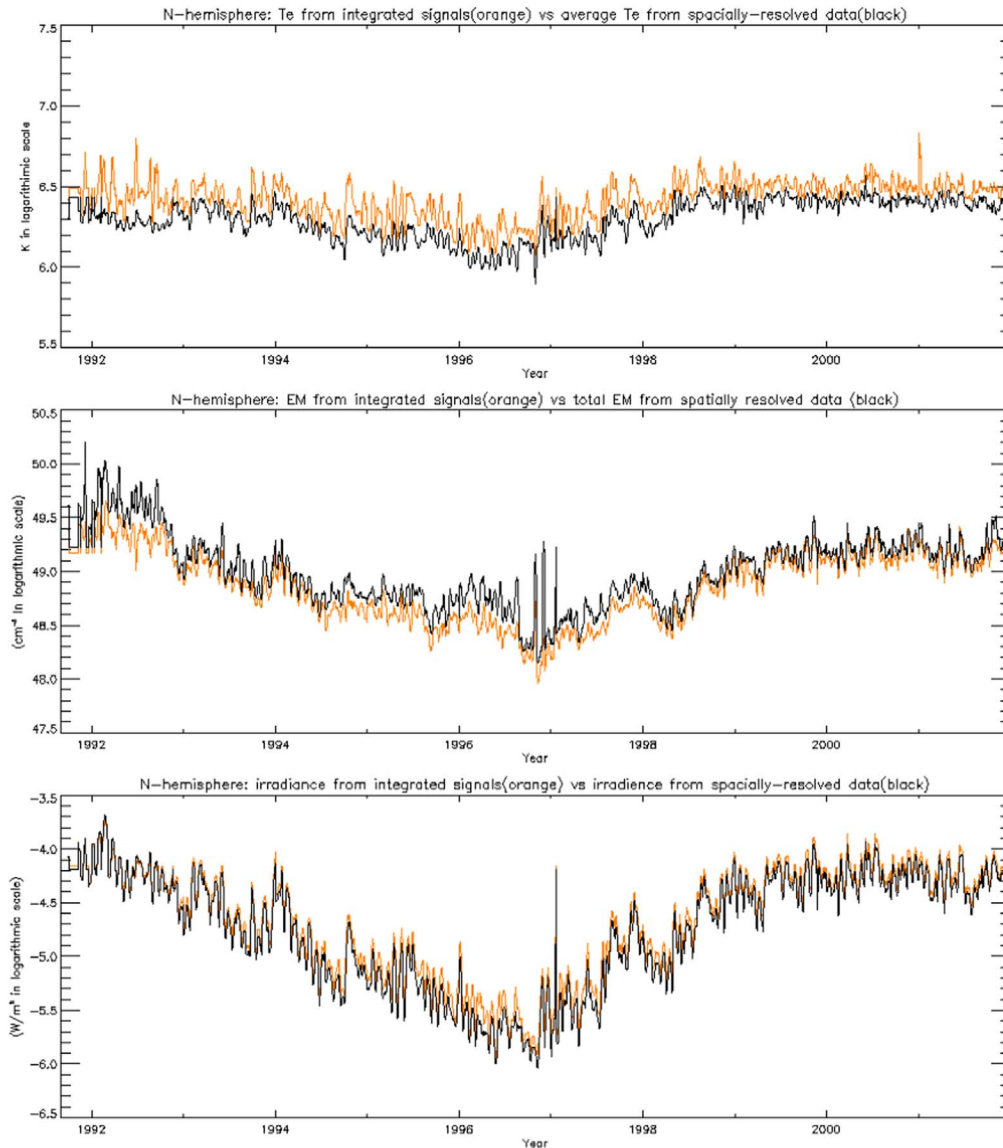
Figure 11. Northern hemispheric coronal temperature (top), emission measure (middle), and irradiance (bottom) obtained from the spatially resolved data (black lines) compared with those from the spatially integrated signals (orange lines). Data points were smoothed by a 7 day running average.

on the contrary, the cooler component contributes to the average through its own EM. When the Sun's activity level was the lowest near the solar minimum, the signals from the dark area of the image turned closer to the level of uncertainty, and started to show spiky noise. Such noise spikes do contribute to raise the filter-ratio temperature derived from the integrated signals (as reported in Section 3.1), but do not contribute much to the averaged temperature from the spatially resolved data as long as the majority of the pixels have an adequate signal-to-noise ratio.

Corresponding to the behavior of the temperatures, the EMs derived from the spatially resolved data are 20%–50% higher outside the period of solar minimum, and a factor of 10–30 higher around the solar minimum (middle plot in Figure 11). These temperatures and EMs calculated from the spatially resolved data make little difference in the level of irradiance except the period of the Sun's lowest activity (bottom plot in Figure 11). The difference outside solar minimum is within 10% relative to the irradiance derived from the integrated signals. Early in 1996, on the other hand, the irradiance from the spatially resolved data are 40%–50% lower than those from

the integrated signals which are more susceptible to the noise in the low signal areas (see the discussion in Section 3.1). Figure 12 presents the above results in the same framework as Figure 5, for the sample years, 1992, 1996, and 2000.

The uncertainty of the temperatures and EMs of the images is generally 3%–5% for the images with the pixel resolution of 9″.8 used for this work. However, a small area with abnormally high uncertainty values coming from the calibration of the stray light often appears in an image and messes up the calculation of the uncertainty of the averaged temperature and total EM. When such an area is masked out, the uncertainty of the averaged temperature and total EM settles down to a comparable level with the corresponding results from the integrated signals.

4.2. Three Temperature Component Analysis

Next, we divided the pixels in each temperature map into three groups; the pixels with a temperature less than 1.5 MK (the cool component), the pixels with a temperature between 1.5 and 2.5 MK (the medium component), and the pixels with a
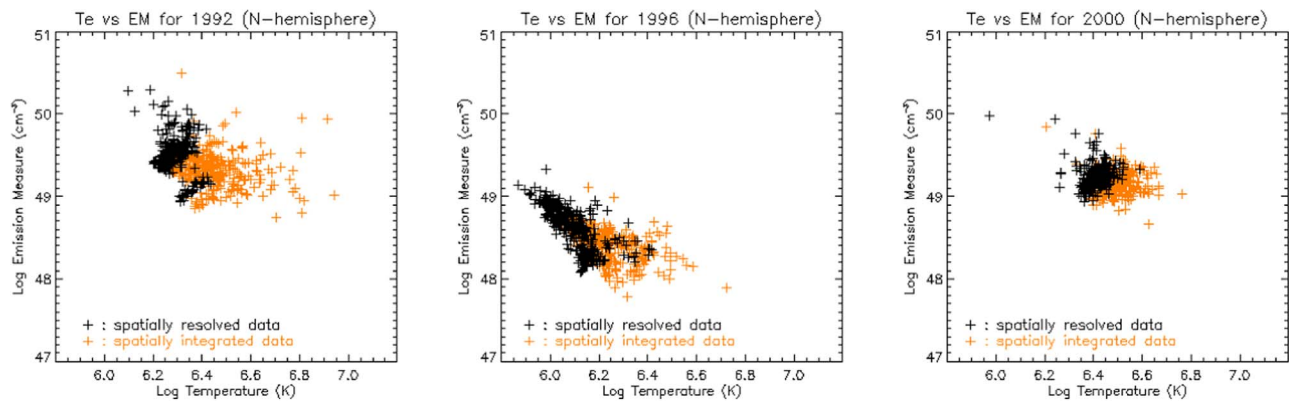
Figure 12. Scatter plots of daily averaged filter-ratio temperatures and emission measures obtained from two different methods. The data points calculated from spatially resolved data (black) are compared with the data points calculated from spatially integrated signals (orange). These results are for the northern hemisphere for the sample years, 1992 (left), 1996 (middle), and 2000 (right).
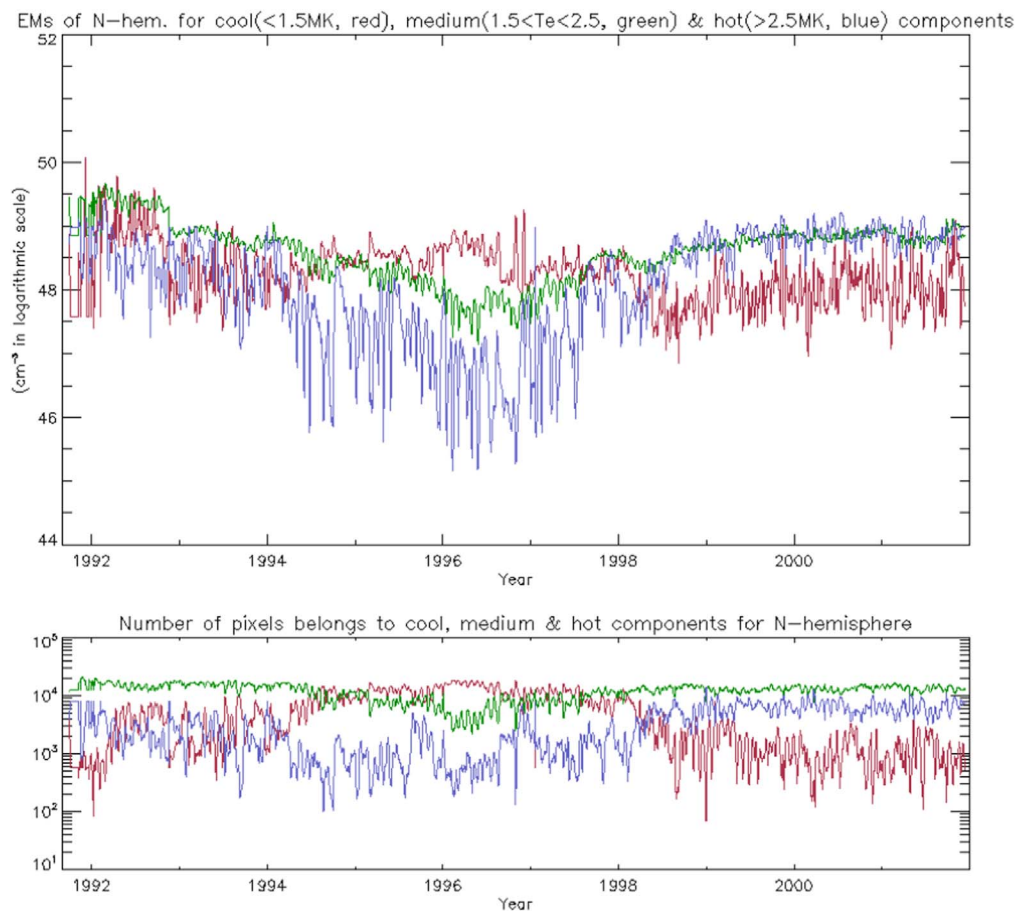

Figure 13. Top plot: mission-long variation of the emission measures of the cool (red), medium (green) and hot (blue) components of the northern hemispheric corona. See the text for a definition. Bottom plot: variation of the number of pixels that belongs to each temperature component of the above plot. Data points of both plots were smoothed by a 5 day running average.

temperature higher than 2.5 MK (the hot component). We then used the corresponding EM map to obtain the total EM of the pixels that belong to each component. The mission-long variations of the EMs of cool, medium, and hot components are plotted in Figure 13. The variation of number of pixels that belongs to each temperature component is also plotted in Figure 13. Figure 14 demonstrates the distributions of the spatially resolved EMs obtained from a single filter pair taken on typical days in 1992, 1996, and 2000, together with the

coronal images with the Al.1 filter and the area in the northern hemisphere used in the analysis.

While the medium and hot components show a similar curve as the irradiance (bottom plot in Figure 11), the cool component in Figure 13 appears to increase roughly by a factor of 10 in early 1996 when the solar activity is around minimum. However, this enhancement is likely to be caused by the under-correction of the stray light component on the Al.1 filter images, because the stray light correction is very difficult
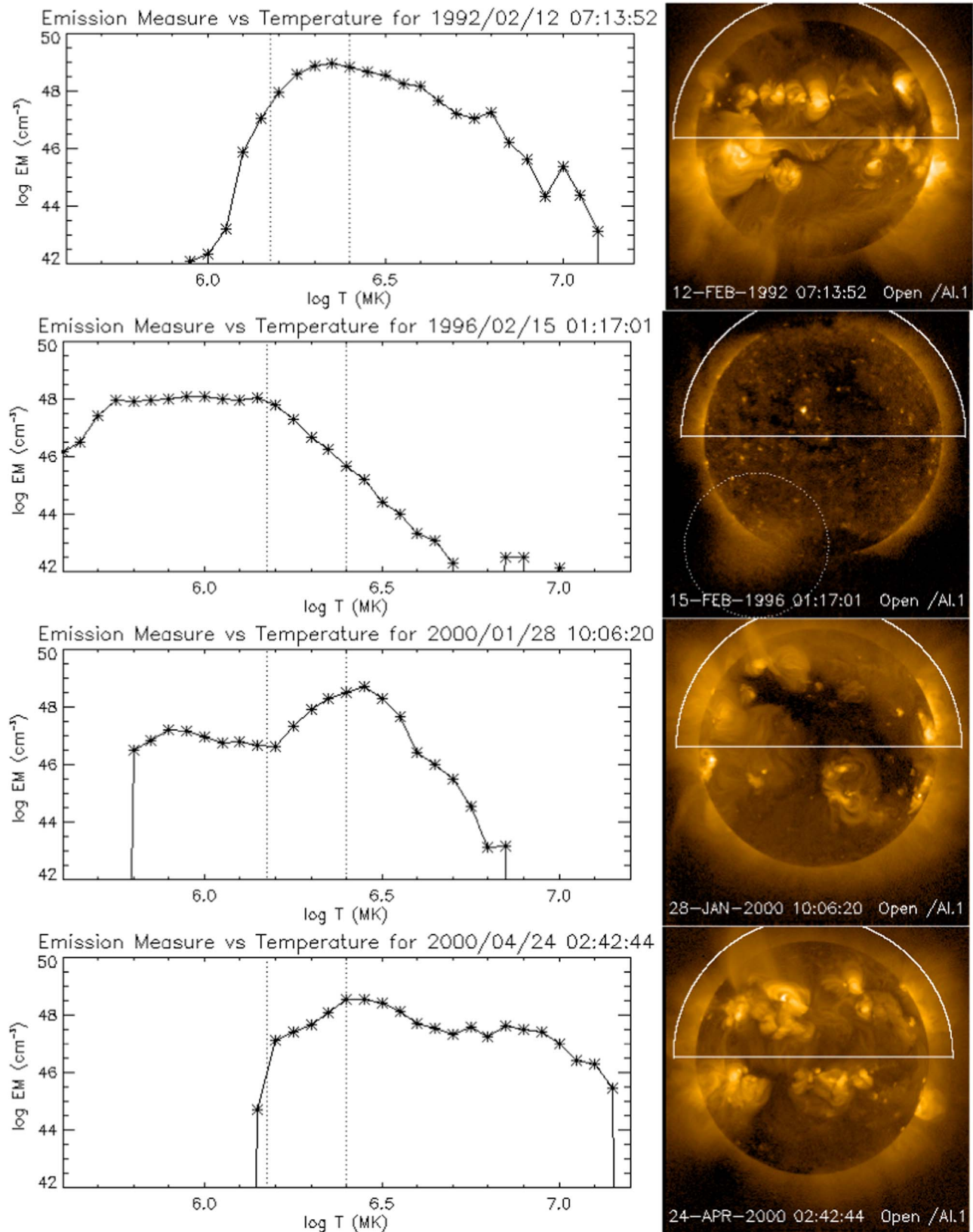
Figure 14. Distribution of spatially resolved emission measures with temperature (bin size $\Delta \log T = 0.05$ MK) obtained from the northern hemispheric corona on a typical day in 1992 (top plot), 1996 (second plot), 2000 January (third plot), and 2000 April (bottom plot). The vertical dotted lines indicate the boundary temperatures of the cool, medium, and hot components defined in this work. The coronal images on the right are the Al.1 filter images used to derive the plots on the left. The white solid line is the boundary of the area where the signals were collected. The stray light correction is imperfect in the 1996 image, presenting with a bright blob in the SE quadrant (white dotted circle in the 1996 image), while it is slightly over-corrected in the 2000 April image.

in this period due to the low signal level of the corona. Since the current method of stray light calibration is not optimized for this period, we need further analysis to discuss the minimum state of the corona. In the same vein, the 1996 plot of Figure 14 should be interpreted with caution. The distribution of the cool component may be corrected by the improvement of the stray light calibration.

Outside this tricky period, the EMs of each temperature component are more reliable and worth discussing. The cool component dominates other components until mid 1997, then drops rapidly during the year of 1998. This is a similar trend to that of observed coronal hole area reported by Lowder et al. (2017) with *Solar and Heliospheric Observatory*/EIT observations. According to their Figure 3, the strong polar magnetic field of the Solar Cycle 23 disappears rapidly in 1998. It is reasonable to associate the variation of cool component with the evolution of coronal hole area, as a source region of cool plasma. However, it is the quiet Sun corona that contributes substantially to the cool component observed by the SXT. It is typically shown in the 1996 plot of Figure 14, when the strong polar coronal hole does not affect much to the EMs observed by SXT. The coronal holes appeared at low latitude do contribute to the cool component (see the 2000 January plot in Figure 14), but their effect is mild due to their low EM. They will rather contribute through the depletion of hot plasma in the observed corona. We do not recognize the immediate relation between the temporal variation of the cool component observed by SXT and that of low-latitude coronal hole area reported by Lowder et al. (2017). Our data in Figure 13 is only for the northern hemisphere, but the result differs little when we use the whole Sun area.

The total EM of the hot component in the descending phase of activity cycle (1992–1995) is significantly lower than that of the medium component, while in the ascending phase, especially from mid-1998 to 2001, the amount of the hot component is comparable with that of the medium component. This indicates that the corona in the ascending phase contains more of the hot plasma than that in the descending phase. The same view is demonstrated in Figure 14 with the larger amount of hot component plasma (especially over 6.8 MK) in the 2000 April corona than in the 1992 corona. According to the bottom plot of Figure 13, on the other hand, the number of hot component pixels is significantly larger in the ascending phase than in the descending phase. Therefore, the increased ratio of the hot component plasma in the ascending phase is explained mainly by the expansion of the hot temperature region rather than by the appearance of the active regions hotter than those in the descending phase. The suggested description of the corona for this period is that a larger number of active regions appeared in the observed area, or the temperature of the quiet Sun corona is higher compared with their counterparts in the descending phase. Both cases are consistent with the observation by SXT, but the statistical confirmation of this view is beyond the scope of this work.

We see an unnatural gap in late 1992, especially in the medium temperature component. We consider that our latest calibration on the contamination on the prefilter and the first prefilter failure event (Acton 2018) is still insufficient at least for the northern hemispheric area of the data. We performed the same analysis using spatially resolved full-Sun images, and confirmed that the overall trend was unchanged.

5. Summary

The soft X-ray irradiance of the Sun in the wavelength range of 0.3–3.0 nm was calculated for the period 1991 September–2001 December, using the mission-long Yohkoh/SXT full-Sun X-ray images found in the YLA. The irradiance was calculated from the filter-ratio temperatures and EMs of the integrated signals of the area within $1.2R_\odot$ with the use of coronal spectra synthesized with CHIANTI atomic database version 8.0. These SXT irradiance data are open to the public from the YLA at the following URL. http://ylstone.physics.montana.edu/ylegacy/yla_sxirrad_acv/yla_sxirrad_acv.html.

The daily averaged values of mission-long filter-ratio temperature and EMs were discussed as functions of $\log Te$ (K) and $\log EM$ (cm^{-3}). The data points in 1992 (near the solar maximum) are located at the area centered at (6.5, 49.5), moving toward around (6.25, 48.7) in 1996 (near the solar minimum) then turning back to the previous values at the maximum phase in 2000. Our calculation is based on the elemental abundances proposed by Schmelz et al. (2012), which is the latest version of the so-called "hybrid" abundances. By assuming traditional coronal abundances by Feldman et al. (1992), the temperatures show no significant difference, while the EMs result in 30%–45% lower values. The resulting irradiance has no significant difference or less than 5% higher values compared with the irradiance obtained with the hybrid abundances. The effect of the assumption of the photospheric abundances by Caffau et al. (2011) was also investigated.

We calculated the soft X-ray irradiance for the shorter wavelength range similar to *GOES*/XRS for the purpose of comparison. We found that the SXT irradiance calculated for the range 0.1–1.0 nm yields the closest flux level to the *GOES*/XRS long channel flux (0.1–0.8 nm) when the solar activity was medium to high. Around the solar minimum, the flux from *GOES*/XRS went under the detection limit for most of the time, while the SXT signals still hold valid information. We therefore consider that the SXT irradiance can be used as the correction of the *GOES*/XRS flux around the period of solar minimum.

For the purpose of incorporating the spatial information to the irradiance study, we tried an alternative method to derive the irradiance by applying the filter-ratio method to the coronal images instead of spatially integrated signals. We used only northern hemispheric data which is less effected by stray light contamination, and compared the results with the corresponding results obtained from the integrated signals. It turned out that the EM weighted average of the spatially resolved temperatures are generally 20%–30% lower than those derived from the integrated signals, while the total of spatially resolved EMs are accordingly 1.5–2 times higher. These trends are enhanced when solar activity is in the lowest level in early 1996, because of the increased number of low signal-to-noise pixels, whose spike noise contributes more to the results using integrated signals than to those with spatially resolved data. The SXT irradiance calculated from the spatially resolved data is within 10% difference from the one derived from the spatially integrated signals, but near the solar minimum, the irradiance from spatially resolved data is 50% lower than that from the integrated signals. The different results from the two approaches suggest an interesting perspective on the interpretation of other stellar data.

Using the spatially resolved information of temperature and EM of the corona, we derive the mission-long variation of the total EMs of cool (less than 1.5 MK), medium (1.5–2.5 MK), and hot (more than 2.5 MK) temperature components. It is

noticed that the cool component increases in early 1996 when the solar activity was around minimum, while the medium and hot components show the similar curve as the irradiance. However, this result highly depends on the quality of stray light calibration, and needs to be confirmed by the more detailed analysis. It is also noticed that the total EM of the hot component in the ascending phase of the solar activity cycle (especially since mid-1998) rises to the comparable level with that of the medium component. In the ascending phase, on the contrary, the amount of the hot component is significantly lower than that of medium component. Considering the fact that the larger amount of hot component in the ascending phase is accompanied by the increased number (or area) of hot component pixels, it is caused by the more number of active regions and/or higher temperature of the quiet Sun than the descending phase.

References

Acton, L. W. 2016, SoPh, 291, 643A
Acton, L. W. 2018, SoPh, 293, 137A
Acton, L. W., Weston, D. C., & Bruner, M. E. 1999, JGR, 104, 14827
Brooks, D. H., Baker, D., van Driel-Gesztelyi, L., & Warren, H. P. 2017, NatCo, 8, 183
Bruner, M. E., & McWhirter, R. W. P. 1988, ApJ, 326, 1002B
Caffau, E., Ludwig, H. G., Steffen, M., Freytag, B., & Bonifacio, P. 2011, SoPh, 268, 255C
Del Zanna, G., Dere, K. P., Young, P. R., Landi, E., & Mason, H. E. 2015, A&A, 582, 56D
Feldman, U., Mandelbaum, P., Seely, J. F., Doschek, G. A., & Gursky, H. 1992, ApJS, 81, 387
Freeland, S. L., & Handy, B. N. 1998, SoPh, 182, 497F
Hara, H., Tsuneta, S., Lemen, J. R., Acton, L. W., & McTiernan, J. M. 1992, PASJ, 44, 135
Lowder, C., Qiu, J., & Leamon, R. 2017, SoPh, 292, 18L
Mewe, R., Gronenschild, E. H. B. M., & van den Oord, G. H. J. 1985, A&AS, 62, 197M
Mewe, R., Lemen, J. R., & van den Oord, G. H. J. 1986, A&AS, 65, 511M
Ogawara, Y., Takano, T., Kato, T., et al. 1991, SoPh, 136, 1
Peres, G., Orlando, S., Reale, F., et al. 2000, ApJ, 528, 537P
Schmelz, J. T., Reames, D.-V., von Steiger, R., & Basu, S. 2012, ApJ, 755, 33
Takeda, A. 2011, SoPh, 273, 295T
Takeda, A., Acton, L., McKenzie, D., Yoshimura, K., & Freeland, S. 2009, DatSJ, 8, PIGY1
Tsuneta, S., Acton, L., Bruner, M., et al. 1991, SoPh, 136, 37T